

# Simulation of the optical properties of plate aggregates for application to the remote sensing of cirrus clouds

Yu Xie,<sup>1,\*</sup> Ping Yang,<sup>1</sup> George W. Kattawar,<sup>2</sup> Bryan A. Baum,<sup>3</sup> and Yongxiang Hu<sup>4</sup>

<sup>1</sup>Department of Atmospheric Sciences, Texas A&M University, College Station, Texas 77843, USA

<sup>2</sup>Department of Physics and Astronomy, Texas A&M University, College Station, Texas 77843, USA

<sup>3</sup>Space Science and Engineering Center, University of Wisconsin–Madison, Madison, Wisconsin 53706, USA

<sup>4</sup>NASA Langley Research Center, Hampton, Virginia 23681, USA

\*Corresponding author: xieyupku@tamu.edu

Received 21 July 2010; revised 21 December 2010; accepted 10 January 2010;  
posted 12 January 2011 (Doc. ID 131964); published 2 March 2011

In regions of deep tropical convection, ice particles often undergo aggregation and form complex chains. To investigate the effect of the representation of aggregates on electromagnetic scattering calculations, we developed an algorithm to efficiently specify the geometries of aggregates and to compute some of their geometric parameters, such as the projected area. Based on *in situ* observations, ice aggregates are defined as clusters of hexagonal plates with a chainlike overall shape, which may have smooth or roughened surfaces. An aggregate representation is developed with 10 ensemble members, each consisting of between 4–12 hexagonal plates. The scattering properties of an individual aggregate ice particle are computed using either the discrete dipole approximation or an improved geometric optics method, depending upon the size parameters. Subsequently, the aggregate properties are averaged over all geometries. The scattering properties of the aggregate representation closely agree with those computed from 1000 different aggregate geometries. As a result, the aggregate representation provides an accurate and computationally efficient way to represent all aggregates occurring within ice clouds. Furthermore, the aggregate representation can be used to study the influence of these complex ice particles on the satellite-based remote sensing of ice clouds. The computed cloud reflectances for aggregates are different from those associated with randomly oriented individual hexagonal plates. When aggregates are neglected, simulated cloud reflectances are generally lower at visible and shortwave-infrared wavelengths, resulting in smaller effective particle sizes but larger optical thicknesses. © 2011 Optical Society of America

OCIS codes: 010.0280, 010.1310, 010.1615.

## 1. Introduction

In recent years, significant research has been performed to improve the representation of the bulk-scattering and absorption properties of ice clouds within the atmosphere. Ice cloud bulk-scattering models have been developed by Baum *et al.* [1,2] for remote sensing applications from visible (VIS) through infrared (IR) wavelengths, and the ice clouds were assumed to be composed of ice crystals with a

set of idealized particle habits, i.e., solid bullet rosettes, solid and hollow columns, droxtals, aggregates of solid columns, and hexagonal plates. The release of new microphysical ice cloud data from *in situ* measurements [3,4] suggests that the representation of complex particles needs modification, such as in the bullet rosette and aggregate models. The conventional solid bullet rosettes have been modified to have a hollow structure at the end of the columnar part of each bullet branch [5]. In addition to homogeneous ice particles, ice crystals with hexagonal habits were observed to contain internal air bubbles with spherical or spheroidal geometries [6].

Furthermore, due to collisions with water droplets or other ice cloud particles during the formation process, nonspherical ice crystals in ice cloud models are regarded as more realistic when their surfaces are not assumed to be perfectly smooth. The scattering of radiation by nonspherical ice crystals with rough surfaces has been discussed by Macke *et al.* [7], Yang and Liou [8], Shcherbakov *et al.* [9], and Yang *et al.* [10,11].

The representation of aggregated ice particles in cloud studies is an area needing further refinement and clarification. Aggregates are frequently found in regions of deep tropical convection [12–23] and are responsible for the generation and growth of precipitation particles that may coexist with supercooled water droplets at temperatures warmer than  $-30^{\circ}\text{C}$  [12]. Ice particles grown in supersaturated air fall through the atmosphere at various speeds. Although the exact mechanism for aggregate formation is not well understood [17], ice particles can form aggregates from collisions resulting from the relative motion and aerodynamic interactions or in the presence of a strong electric field. Aggregation is significantly influenced by the presence of strong electric fields that tend to exist in clouds with strong updrafts [24]. It has also been suggested that ice particles within tropical convective clouds are more likely to form aggregates in the presence of an electric field [13,17,25].

The coalescence rate is related to the habits of the individual ice particles and the ambient cloud temperature. Extensive laboratory studies (e.g., Hobbs *et al.* [26]) have demonstrated that hexagonal ice crystals that form at relatively warm temperatures (between  $-10^{\circ}\text{C}$  and  $-15^{\circ}\text{C}$ ) may increase the aggregation rate. Furthermore, individual ice aggregates have often been found to be chains of plate-shaped crystals [13,27].

Current ice cloud bulk-scattering and absorption models used in the operational Moderate Resolution Imaging Spectroradiometer (MODIS) cloud property retrievals involve a percentage of roughened aggregates with large maximum dimensions [1,2]. A specific aggregate geometry defined by Yang and Liou [8], includes eight hexagonal columns. The aggregate dimension can be scaled when each hexagonal column is enlarged or reduced while the aspect ratio is kept invariant. The ice aggregate model was modified into a chainlike aggregate by Baran and Labonnote [28] and used for remote sensing applications based on Polarization and Directionality of Earth's Reflectances data. The original model was transformed into the chainlike aggregates by stretching and rotating two of the original hexagonal columns to make the aggregate particle less dense (i. e., decreasing the volume-to-area ratio) and, therefore, to better fit the *in situ* observations.

Evans *et al.* [20] generated three types of aggregates consisting of 6–40 randomly oriented hexagonal columns and plates. Each aggregate monomer had a predetermined aspect ratio and particle size,

and a larger particle was constructed by interlocking the fixed monomers. The discrete dipole approximation (DDA) method [29–32] was used to compute the scattering properties of the aggregates for application to the simulation of the radiances measured by the Compact Scanning Submillimeter Imaging Radiometer and the Cloud Radar System on NASA's ER-2 aircraft. The aggregate ice particles were represented in the DDA code with each dipole size set to be the thickness of a hexagonal plate monomer. Um and McFarquhar [22] defined geometries of aggregates using ice particles formed from seven hexagonal plates, and the scattering properties of the aggregates were computed by the geometric ray-tracing technique [7,21,22,33,34].

In this study, we define a new set of aggregate ice particles made from plates and investigate the scattering properties from VIS to IR wavelengths. A computationally efficient method is presented in Section 2 to generate numerical aggregate geometries that are similar to those obtained from *in situ* measurements. In Section 3, we develop an aggregate representation from an ensemble of aggregate geometries and compute the resulting scattering properties. Section 4 is a discussion of the capability of the aggregate representation to represent general aggregates within ice clouds. The influence of the aggregate particles on the remote sensing of ice cloud microphysical and optical properties is discussed in Section 5, and conclusions are provided in Section 6.

## 2. Numerical Models for the Aggregation of Hexagonal Ice Crystals

The geometries of aggregate ice particles are available from *in situ* data collected during field campaigns [12–18,20]. Based on observations and on the formation processes, aggregates most likely contain hexagonal monomers. Furthermore, the aggregates tend to contain significantly more hexagonal plates than columns, indicating the cloud temperatures corresponding to the formation of the ice particles. The hexagonal ice monomers vary in the aspect ratio, and they can be attached together in planar and in more complex three-dimensional forms. Thus, one specific aggregate geometry will be insufficient to realistically represent natural aggregates. However, as demonstrated by Stith *et al.* [13], aggregates of plates often exhibit chain-style shapes instead of more compact shapes.

In the present study, the geometries of aggregates are defined by attaching hexagonal plates together in a chain-style structure. The monomer plates are in random orientations in the aggregates. The aspect ratios of the hexagonal plates, representing the relationship between the width and length of the particle, follow the *in situ* measurements reported by Pruppacher and Klett [35]. For a hexagonal plate larger than  $5\mu\text{m}$ , the aspect ratio is determined by the relationship [35]:

$$L = 2.4883\alpha^{0.474}, \quad (1)$$

where  $a$  and  $L$  represent the semiwidth and length of the ice crystal, respectively. The units of  $a$  and  $L$  are micrometers. Because aggregates consist of plates with similar sizes,  $a$  in Eq. (1) is given by

$$a = 20 + 20\xi_1, \quad (2)$$

$$a = 40 + 40\xi_2, \quad (3)$$

for generating relatively small and large aggregates, where  $\xi_1$  and  $\xi_2$  are independent random numbers distributed uniformly in  $[0, 1]$ .

Following Yang and Liou [8], we define aggregate ice crystals in a three-dimensional Cartesian coordinate system,  $oxyz$ , where the geometric coordinate of each hexagonal plate can be determined by the width, length, particle-center coordinates, and the Euler angles on the basis of a  $z$ - $y$ - $z$  convention. Figure 1(a) shows an example of a hexagonal particle that is specified in the  $oxyz$  coordinate system (the laboratory system) and in  $o_Px_Py_Pz_P$  (the particle system). The transfer from the particle ( $o_Px_Py_Pz_P$ ) to the laboratory system ( $oxyz$ ) through an intermediate coordinate system ( $ox'_Py'_Pz'_P$ ) is given by

$$\begin{bmatrix} x'_P \\ y'_P \\ z'_P \end{bmatrix} = \begin{bmatrix} x_P \\ y_P \\ z_P \end{bmatrix} + \begin{bmatrix} x'_0 \\ y'_0 \\ z'_0 \end{bmatrix}, \quad (4)$$

$$\begin{bmatrix} x \\ y \\ z \end{bmatrix} = R \begin{bmatrix} x'_P \\ y'_P \\ z'_P \end{bmatrix}, \quad (5)$$

where  $(x'_0, y'_0, z'_0)$  are the coordinates of the origin of the  $o_Px_Py_Pz_P$  system in the  $ox'_Py'_Pz'_P$  coordinate system and  $R$  is a rotational transformation matrix given by

$$\begin{aligned} R &= \begin{bmatrix} \cos \gamma & -\sin \gamma & 0 \\ \sin \gamma & \cos \gamma & 0 \\ 0 & 0 & 1 \end{bmatrix} \cdot \begin{bmatrix} \cos \beta & 0 & \sin \beta \\ 0 & 1 & 0 \\ -\sin \beta & 0 & \cos \beta \end{bmatrix} \cdot \begin{bmatrix} \cos \alpha & -\sin \alpha & 0 \\ \sin \alpha & \cos \alpha & 0 \\ 0 & 0 & 1 \end{bmatrix} \\ &= \begin{bmatrix} \cos \alpha \cos \beta \cos \gamma - \sin \alpha \sin \gamma & -\cos \beta \cos \gamma \sin \alpha - \cos \alpha \sin \gamma & \cos \gamma \sin \beta \\ \cos \gamma \sin \alpha + \cos \alpha \cos \beta \sin \gamma & \cos \alpha \cos \gamma - \cos \beta \sin \alpha \sin \gamma & \sin \beta \sin \gamma \\ -\cos \alpha \sin \beta & \sin \alpha \sin \beta & \cos \beta \end{bmatrix}, \end{aligned} \quad (6)$$

where  $\alpha$ ,  $\beta$ , and  $\gamma$ , respectively, are the Euler angles that represent three consecutive rotations around the  $z$ ,  $y$ , and  $z$  axes. The positive values of the Euler angles indicate clockwise rotations in their rotating planes. To represent aggregates having random orientations, the Euler angles of the coordinate rotations are given by

$$\alpha = \pi(2\xi_3 - 1), \quad (7)$$

$$\beta = \cos^{-1}(2\xi_4 - 1), \quad (8)$$

$$\gamma = \pi(2\xi_5 - 1), \quad (9)$$

where  $\xi_3$ ,  $\xi_4$ , and  $\xi_5$  are independent random numbers uniformly distributed in  $[0, 1]$ . As shown in Fig. 1(a), the valid range of  $\alpha$ ,  $\beta$ , and  $\gamma$  is  $(-\pi, \pi]$ . The particle centers of the hexagonal ice particles are determined in the  $oxyz$  coordinate system by

$$x_0 = d\xi_6 \sin \theta \cos \varphi, \quad (10)$$

$$y_0 = d\xi_6 \sin \theta \sin \varphi, \quad (11)$$

$$z_0 = d\xi_6 \cos \theta, \quad (12)$$

$$\theta = \cos^{-1}(2\xi_7 - 1), \quad (13)$$

$$\varphi = 2\pi\xi_8, \quad (14)$$

where  $d$  is initially set as a large value, e.g.,  $1000 \mu\text{m}$ ;  $\xi_6$ ,  $\xi_7$ , and  $\xi_8$  are independent random numbers distributed uniformly in  $[0, 1]$ ; and  $\theta$  and  $\varphi$  are the polar and azimuthal angles in the  $oxyz$  coordinate system [see Fig. 1(b)].

With the representations of an ice particle in the  $oxyz$  coordinate system, the distance between multiple ice particles can be computed numerically by considering the shortest distances among all the vertices and boundaries of the ice particles. The distance may be reduced with adjustments to the particle-center coordinates of an ice particle [specifically adjusting  $d$  in Eqs. (10)–(12)] while retaining all the other

elements. Two ice particles can join if they do not overlap and the distance between them is negligible. Appendix A provides a detailed procedure for estimating the relative position between two hexagonal particles, computing their distance, and identifying whether or not they are overlapped. Repetition of

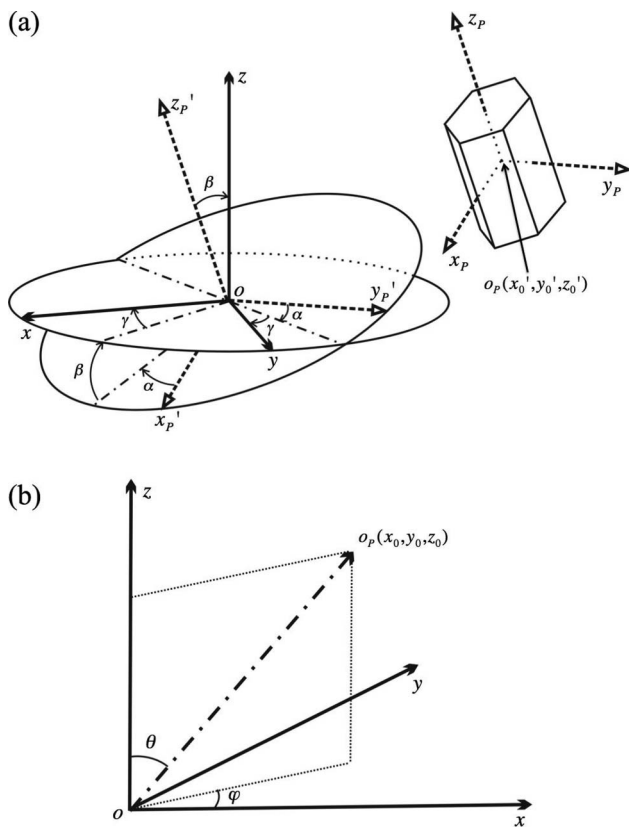


Fig. 1. (a) Transformation from the  $opxpypzp$  to  $oxyz$  coordinate system. (b) Polar and azimuthal angles in the  $oxyz$  coordinate system.

the preceding process attaches more hexagonal plates to the particle. Because of the geometry of the particles, a new particle with determined  $\alpha, L, \alpha, \beta$ , and  $\gamma$  may not necessarily touch some existing aggregate elements. Therefore, the aggregation process begins again by testing the possibility that the aggregate elements can be attached to the new particle. To define chain-style aggregates, the test is performed with the newly attached aggregate elements while the parameters in Eqs. (7)–(9) are revised. For example, let

$$\beta_N = \begin{cases} \cos^{-1}(2\xi_9 - 1) & \text{for } N = 1 \\ \beta_{N-1} + \cos^{-1}[2.0 \times (0.9^{90\xi_{10}} - 0.5)] & \text{for } N > 1 \end{cases} \quad (15)$$

where  $N$  indicates the  $N$ th hexagonal plate in the aggregation process.

Using the aforementioned procedure, we defined the numerous aggregates shown in Figs. 2 and 3. Figure 2 shows samples of “small” aggregates (hereafter referred to as aggregates 1–5) consisting of four or five hexagonal plates. The dimensions of the aggregates in Fig. 2 can be scaled to fit the size parameters involved in the single-scattering computations. However, as suggested by recent *in situ* measurements [3,4,20], aggregates with extremely large particle sizes are achieved by increasing the

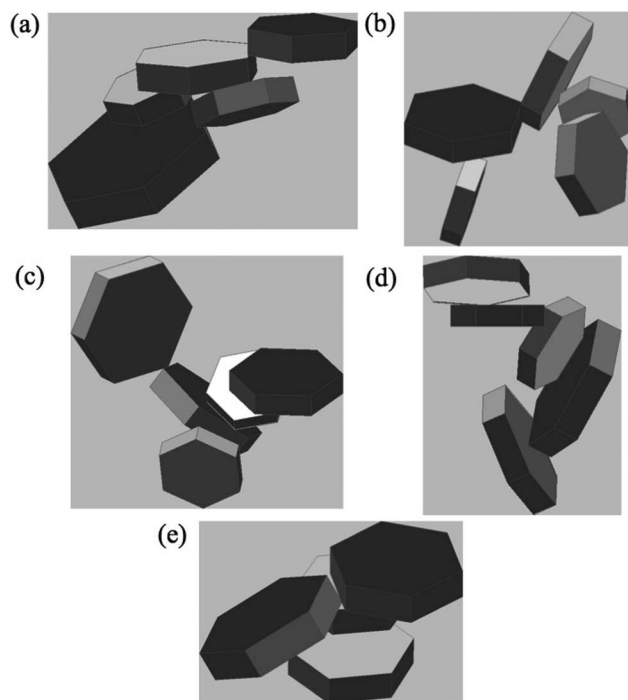


Fig. 2. Geometries of aggregates: (a) 1, (b) 2, (c) 3, (d) 4, and (e) 5.

monomer numbers instead of only scaling the sizes of each monomer. As shown in Fig. 3, “large” aggregates are represented by five models (hereafter referred to as aggregates 6–10), each consisting of 8–12 hexagonal plates. In general, the ice cloud effective particle size for a given particle size distribution

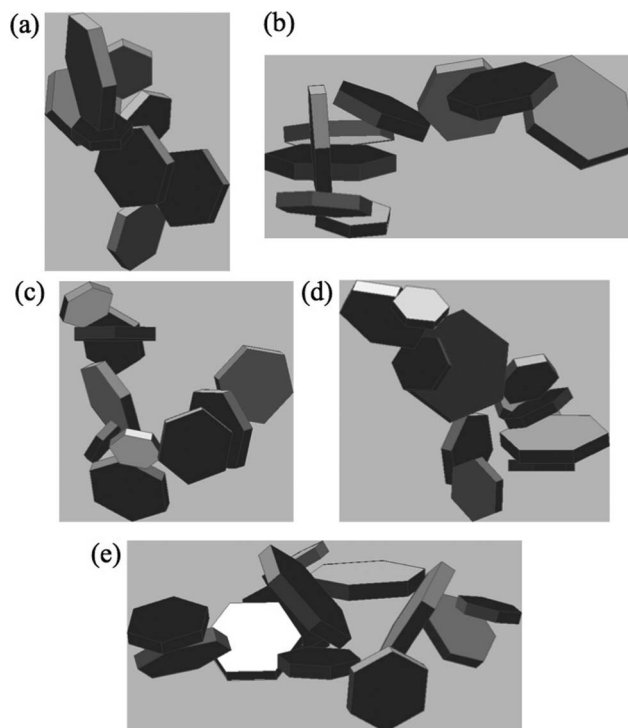


Fig. 3. Geometries of aggregates: (a) 6, (b) 7, (c) 8, (d) 9, and (e) 10.



is defined by the maximum dimensions  $D_m$ , projected areas  $A$ , and volumes  $V$  of the individual particles. Counting the largest distance between all the aggregate vertices determines the maximum dimensions of the aggregates shown in Figs. 2 and 3. An algorithm based on the Monte Carlo method computes the projected areas of the aggregates, and the details are provided in Appendix B.

Figures 4(a) and 4(b) illustrate the ice crystal projected area and volume, respectively, for aggregates 1–5 as functions of the particle maximum dimension. Among the five habits used to represent small aggregates, aggregate 2 has a significantly larger projected area than the other habit realizations. Aggregate 5 has the smallest and largest values of projected area and volume, respectively, which indicates a much more compact aggregate. Aggregate 4 exhibits a less compact particle compared to aggregates 1, 3, and 5 and has a smaller volume and a larger projected area than the other habits. Figures 4(c) and 4(d) show the particle projected area and volume for aggregates 6–10. For aggregates having the same particle sizes, aggregates 7 and 9 have very similar volumes, whereas their projected areas are much smaller than those of the other habits. However, the volume of aggregate 10 is not distinct from aggregates 7 and 9. The para-

meters associated with the aggregates in Figs. 2 and 3 can be found in Tables 1 and 2.

### 3. Scattering Properties of Aggregates

The scattering properties of the small and large aggregates are computed by a combination of the ADDA code [36,37] based on the DDA method [29,30,38,39] and an IGOM [40]. The DDA is a technique to accurately simulate electromagnetic scattering by nonspherical particles over a wide frequency range. In the DDA method, the scattering particle is defined in terms of a number of electric dipoles. While the electric field within the computational domain is obtained from the incident electromagnetic wave and the interaction of the electric dipoles, the scattering and absorption properties of the scattering particle are derived via a near-to-far-field transformation. Because of its computational efficiency and convenience in the construction of irregular particle morphology, the DDA has been used to investigate light scattering by both oriented and arbitrary distributed particles, including ice particles and aerosols in the atmosphere [20,41–45].

The extinction efficiencies, asymmetry factors, and scattering phase functions [46] derived by the ADDA have been compared with those from Mie theory [36].

Table 1. Parameters Associated with the Five Aggregates with Small Particle Sizes<sup>a</sup>

Aggregate 1: $D_m = 147.95 \mu\text{m}$ , $A = 5.32057\text{E} + 03 \mu\text{m}^2$ , $V = 1.15867\text{E} + 05 \mu\text{m}^3$								
Element #	$a$	$L$	$\alpha$ (°)	$\beta$ (°)	$\gamma$ (°)	$x_0$	$y_0$	$z_0$
1	24.000	11.223	0.000	0.000	0.000	0.000	0.000	0.000
2	27.000	11.868	-82.655	175.767	-78.103	-5.664	43.934	-13.203
3	22.000	10.770	-7.651	-23.688	-132.443	-13.519	21.792	-25.347
4	20.000	10.294	-101.850	155.069	-50.709	18.656	68.178	-29.741
5	38.000	13.955	-118.412	-30.374	-42.438	-3.161	71.109	-54.738
Aggregate 2: $D_m = 149.21 \mu\text{m}$ , $A = 9.71958\text{E} + 03 \mu\text{m}^2$ , $V = 1.48618\text{E} + 05 \mu\text{m}^3$								
Element #	$a$	$L$	$\alpha$ (°)	$\beta$ (°)	$\gamma$ (°)	$x_0$	$y_0$	$z_0$
1	35.000	13.421	0.000	0.000	0.000	0.000	0.000	0.000
2	35.000	13.421	-136.864	111.886	20.422	37.806	35.423	31.105
3	22.000	10.770	129.602	-103.763	123.851	54.186	51.254	4.438
4	26.000	11.657	-106.007	74.775	-150.946	19.071	-23.051	-32.585
5	30.000	12.476	102.088	-111.157	13.492	70.653	26.702	-12.658
Aggregate 3: $D_m = 162.32 \mu\text{m}$ , $A = 7.26631\text{E} + 03 \mu\text{m}^2$ , $V = 1.77345\text{E} + 05 \mu\text{m}^3$								
Element #	$a$	$L$	$\alpha$ (°)	$\beta$ (°)	$\gamma$ (°)	$x_0$	$y_0$	$z_0$
1	33.000	13.052	0.000	0.000	0.000	0.000	0.000	0.000
2	25.000	11.443	-104.323	147.168	29.018	7.916	31.004	-17.561
3	37.000	13.779	-66.295	-39.138	139.772	4.977	59.195	-37.719
4	26.000	11.657	-117.000	101.552	-154.612	-26.415	41.781	-56.674
5	38.000	13.955	-89.474	-95.683	-111.998	-12.506	99.011	17.501
Aggregate 4: $D_m = 174.08 \mu\text{m}$ , $A = 8.72443\text{E} + 03 \mu\text{m}^2$ , $V = 1.66768\text{E} + 05 \mu\text{m}^3$								
Element #	$a$	$L$	$\alpha$ (°)	$\beta$ (°)	$\gamma$ (°)	$x_0$	$y_0$	$z_0$
1	25.000	11.443	0.000	0.000	0.000	0.000	0.000	0.000
2	26.000	11.657	-136.348	117.880	-25.069	29.954	28.576	-14.725
3	39.000	14.128	-74.542	-63.550	12.115	43.180	44.478	-38.725
4	35.000	13.421	-178.069	113.773	164.661	14.393	57.944	-71.778
5	30.000	12.476	-46.679	165.030	-89.502	-11.329	-2.432	18.621
Aggregate 5: $D_m = 101.73 \mu\text{m}$ , $A = 2.18089\text{E} + 03 \mu\text{m}^2$ , $V = 6.82456\text{E} + 04 \mu\text{m}^3$								
Element #	$a$	$L$	$\alpha$ (°)	$\beta$ (°)	$\gamma$ (°)	$x_0$	$y_0$	$z_0$
1	25.000	11.443	0.000	0.000	0.000	0.000	0.000	0.000
2	27.000	11.868	-22.406	30.910	117.028	-44.627	18.399	-13.063
3	21.000	10.535	-100.936	-179.061	44.979	-2.087	20.477	-18.406
4	23.000	10.999	-135.880	177.983	71.613	-19.081	3.495	-29.831

<sup>a</sup>The units of  $a$ ,  $L$ , and  $(x_0, y_0, z_0)$  are micrometers.

Table 2. Parameters Associated with the Five Aggregates with Large Particle Sizes<sup>a</sup>

Aggregate 6: $D_m = 369.63 \mu\text{m}$ , $A = 3.91496\text{E} + 04 \mu\text{m}^2$ , $V = 1.06798\text{E} + 06 \mu\text{m}^3$								
Element #	$a$	$L$	$\alpha (^{\circ})$	$\beta (^{\circ})$	$\gamma (^{\circ})$	$x_0$	$y_0$	$z_0$
1	40.000	14.298	0.000	0.000	0.000	0.000	0.000	0.000
2	79.000	19.741	-46.217	88.822	11.433	-12.564	13.110	84.021
3	43.000	14.797	-179.796	-93.563	85.646	32.092	34.451	70.872
4	59.000	17.190	-7.572	77.85	-132.999	42.693	0.1521	-57.088
5	49.000	15.742	-25.814	88.721	-49.824	44.632	-4.197	-156.989
6	58.000	17.052	-133.723	-138.154	-47.923	-14.287	75.580	-5.949
7	55.000	16.628	170.641	-62.393	51.869	116.120	16.863	-106.819
8	46.000	15.277	-59.226	86.727	125.394	67.638	95.060	-50.351
Aggregate 7: $D_m = 473.71 \mu\text{m}$ , $A = 2.17697\text{E} + 04 \mu\text{m}^2$ , $V = 1.89471\text{E} + 06 \mu\text{m}^3$								
Element #	$a$	$L$	$\alpha (^{\circ})$	$\beta (^{\circ})$	$\gamma (^{\circ})$	$x_0$	$y_0$	$z_0$
1	78.000	19.623	0.000	0.000	0.000	0.000	0.000	0.000
2	68.000	18.387	82.921	164.510	102.946	-6.719	-54.101	25.823
3	67.000	18.258	-92.660	-22.959	1.713	-60.934	-25.493	57.639
4	69.000	18.515	28.655	86.571	-174.082	5.337	114.889	47.891
5	57.000	16.912	160.118	-114.845	-79.650	-158.696	-28.416	72.697
6	59.000	17.190	-61.486	16.746	-99.622	0.291	122.872	-29.215
7	49.000	15.742	-152.577	167.203	-63.528	-29.232	41.204	-58.603
8	66.000	18.129	-40.620	-16.260	-133.618	-207.718	47.738	96.347
9	79.000	19.741	141.896	133.140	-46.151	-291.690	-26.998	58.650
Aggregate 8: $D_m = 439.51 \mu\text{m}$ , $A = 6.64570\text{E} + 04 \mu\text{m}^2$ , $V = 1.92774\text{E} + 06 \mu\text{m}^3$								
Element #	$a$	$L$	$\alpha (^{\circ})$	$\beta (^{\circ})$	$\gamma (^{\circ})$	$x_0$	$y_0$	$z_0$
1	77.000	19.503	0.000	0.000	0.000	0.000	0.000	0.000
2	58.000	17.052	-177.368	64.830	-27.941	99.193	4.561	-7.375
3	75.000	19.261	-146.815	-117.312	-69.303	115.667	8.322	-105.096
4	42.000	14.633	99.056	53.002	77.723	90.671	21.580	-175.875
5	47.000	15.434	13.853	-135.455	33.875	-18.069	47.826	47.262
6	72.000	18.892	-167.855	43.472	-23.762	97.754	-22.864	-249.469
7	45.000	15.119	-108.623	-142.431	-15.595	7.019	-35.116	-189.123
8	65.000	17.998	-51.308	-72.400	-173.509	-14.105	-132.186	-184.875
9	74.000	19.139	-87.353	75.060	-49.382	32.361	-171.149	-155.846
10	70.000	18.641	-98.065	-111.24	25.565	50.082	-228.132	-81.978
Aggregate 9: $D_m = 445.23 \mu\text{m}$ , $A = 2.08749\text{E} + 04 \mu\text{m}^2$ , $V = 1.57522\text{E} + 06 \mu\text{m}^3$								
Element #	$a$	$L$	$\alpha (^{\circ})$	$\beta (^{\circ})$	$\gamma (^{\circ})$	$x_0$	$y_0$	$z_0$
1	48.000	15.589	0.000	0.000	0.000	0.000	0.000	0.000
2	77.000	19.503	150.470	158.669	64.315	16.422	-9.303	36.460
3	50.000	15.893	156.544	-28.559	7.439	-0.981	12.898	79.428
4	51.000	16.043	133.796	143.141	106.479	8.530	110.051	82.220
5	45.000	15.119	15.886	-42.947	-76.896	-21.106	1.340	120.318
6	79.000	19.741	7.484	100.825	85.510	-126.526	-12.425	138.208
7	43.000	14.797	148.401	-80.442	51.002	-183.477	-38.868	140.806
8	57.000	16.912	29.050	79.070	134.321	-103.686	15.369	22.394
9	46.000	15.277	164.668	-104.400	31.959	-103.477	-37.950	-32.759
10	67.000	18.258	102.284	-39.670	-137.843	-241.91	-59.434	209.639
11	40.000	14.298	-20.386	138.140	88.125	-216.237	-146.224	219.446
Aggregate 10: $D_m = 471.42 \mu\text{m}$ , $A = 6.14953\text{E} + 04 \mu\text{m}^2$ , $V = 1.86694\text{E} + 06 \mu\text{m}^3$								
Element #	$a$	$L$	$\alpha (^{\circ})$	$\beta (^{\circ})$	$\gamma (^{\circ})$	$x_0$	$y_0$	$z_0$
1	51.000	16.043	0.000	0.000	0.000	0.000	0.000	0.000
2	53.000	16.338	121.826	79.245	59.939	44.024	-70.931	-27.186
3	75.000	19.261	-119.265	-122.802	131.734	117.027	-44.620	44.158
4	74.000	19.139	168.954	-47.041	130.687	28.929	51.624	67.320
5	49.000	15.742	175.836	130.105	92.497	152.171	-84.018	27.426
6	73.000	19.016	44.989	177.401	-107.193	155.161	74.466	61.031
7	40.000	14.298	85.171	-13.969	154.203	175.293	-111.757	53.939
8	61.000	17.464	128.262	45.585	-151.717	85.657	138.845	10.530
9	59.000	17.190	86.249	-140.248	-143.415	30.315	139.789	-3.023
10	59.000	17.190	17.525	33.540	73.917	-67.218	161.784	-3.566
11	43.000	14.797	-94.888	-148.820	117.310	108.901	146.382	77.028
12	52.000	16.192	72.882	-18.720	22.437	-105.644	147.902	39.572

<sup>a</sup>The units of  $a$ ,  $L$ , and  $(x_0, y_0, z_0)$  are micrometers.

The root mean square (rms) relative errors from the ADDA are quite small for cases when  $m_r < 1.4$ , where  $m_r$  is the real part of the refractive index.

However, the ADDA requires sufficient electric dipoles in the computational domain to resolve detailed geometric features of the scattering particle

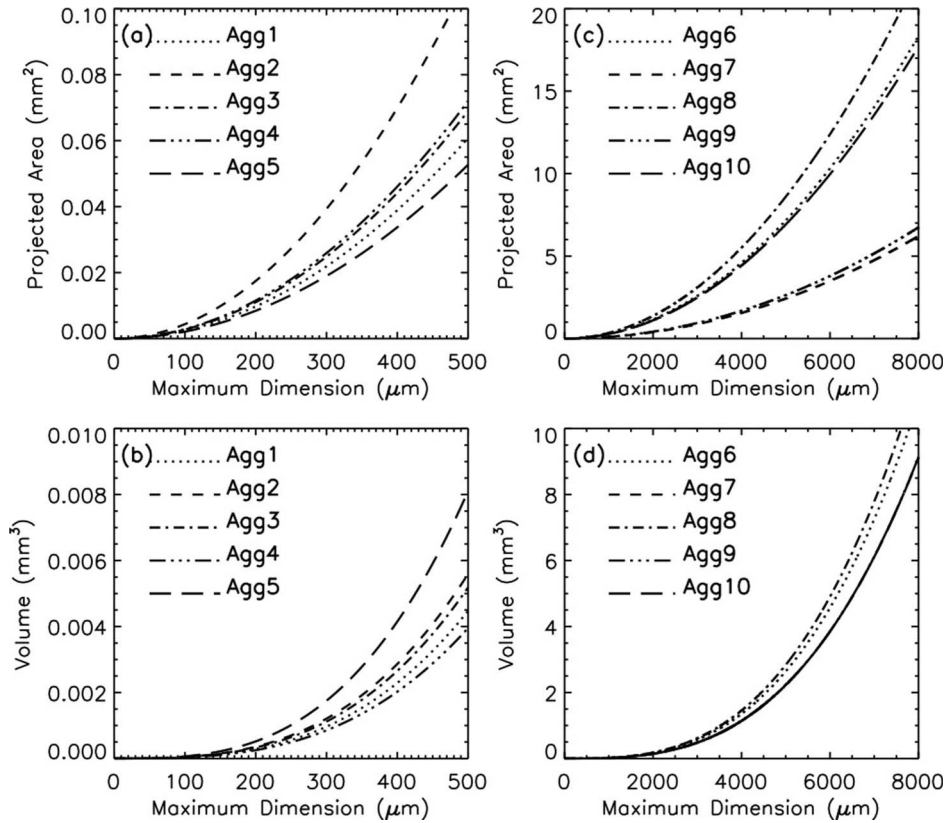


Fig. 4. (a), (b) Variation of ice crystal projected area and volume versus maximum dimension for aggregates 1–5. (c), (d) Variation of ice crystal projected area and volume versus maximum dimension for aggregates 6–10.

and to achieve numerical accuracy. As a result, chained-particle aggregates tend to consume a substantial amount of computing time because of the multiple electric dipoles in a relatively large computational domain. In our study, ADDA v 0.79 [36] is used to compute the scattering properties of aggregates. The size of the electric dipoles in the ADDA is given as follows:

$$d = \begin{cases} \left\langle \frac{D_m}{20}, \frac{\lambda}{20|m|} \right\rangle & \text{for } X \leq 1 \\ \frac{\lambda}{20|m|} & \text{for } 1 < X \leq 5 \\ \frac{\lambda}{10|m|} & \text{for } 5 < X \leq 15 \\ \frac{\lambda}{5|m|} & \text{for } X > 15 \end{cases}, \quad (16)$$

where  $d$  is the interdipole distance,  $m$  is the refractive index of the aggregates,  $\lambda$  is the wavelength, and  $\langle \rangle$  indicates the minimum value of the variables. The size parameter,  $X$ , of an aggregate is defined by

$$X = \frac{\pi D_s}{\lambda}, \quad (17)$$

where  $D_s$  is the diameter of a volume-equivalent sphere. Based on Yurkin and Hoekstra [37], the accuracy of the results decreases with the increase of  $d$  and is reported as several percent when  $d = \frac{\lambda}{10|m|}$ .

The conventional IGOM has been extensively employed in the light scattering and radiative transfer

processes for satellite-based remote sensing of ice clouds [1,2,47–50]. For computations involving large size parameters, the IGOM is an efficient method for computing the scattering properties of aggregates, and our version has been updated in numerous ways over the past few years. Compared to the computations reported by Yang and Liou [8], the current IGOM has improved the treatment of the edge effect [51–53] and enhanced the treatment of forward scattering [42] to more accurately account for the divergence of scattered energy in the forward peak. The result of the new treatment of forward scattering is that a delta-transmission term is no longer required, even for extremely large particles. As a result of the scattering model improvements, the extinction efficiency of an ice particle exhibits a smooth transition from small to large particles whose scattering properties are computed from the ADDA and IGOM, respectively. The IGOM code used in Yang and Liou [8] has been revised to adapt to various sets of parameters associated with aggregates.

Figure 5 shows the extinction efficiency, absorption efficiency, single-scattering albedo, and asymmetry factor as functions of the size parameter for the randomly oriented aggregate 1 at  $\lambda = 2.13 \mu\text{m}$ . The random orientations of the particles are achieved in the ADDA by using the built-in orientation averaging algorithm. A detailed discussion of the averaging process can be found in the literature [36]. The extinction and absorption efficiencies calculated with

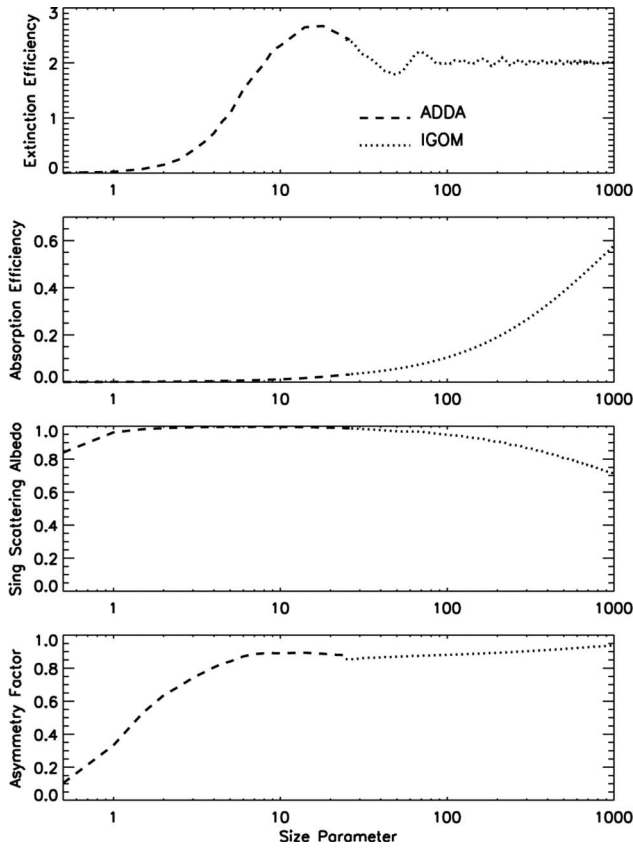


Fig. 5. Extinction efficiency, absorption efficiency, single-scattering albedo, and asymmetry factor as functions of the size parameter for aggregate 1 at  $\lambda = 2.13 \mu\text{m}$ . The refractive index of ice at  $\lambda = 2.13 \mu\text{m}$  is  $1.2673 + i5.57 \times 10^{-4}$ .

the ADDA were originally derived by dividing the corresponding extinction and absorption cross sections of the scattered particle over the cross section of a volume-equivalent sphere. To be more consistent with the IGOM, we replace the cross section of the volume-equivalent sphere by a projected area computed by the process described in Appendix B. In the IGOM computations, the above-edge effect contribution to the extinction and absorption efficiencies can be approximated following Bi *et al.* [42]:

$$Q_{e,\text{edge}}(\lambda) = 2c_1 \left( \frac{\lambda}{\pi D_m} \right)^{2/3}, \quad (18)$$

$$Q_{a,\text{edge}}(\lambda) = 2c_2 \left( \frac{\lambda}{\pi D_m} \right)^{2/3}. \quad (19)$$

The two constants,  $c_1$  and  $c_2$ , are determined by the wavelength ( $\lambda_t$ ) where the ADDA model switches to the IGOM:

$$c_1 = 0.5[Q_{e,\text{ADDA}}(\lambda_t) - Q_{e,\text{IGOM}}(\lambda_t)] \left( \frac{\pi D_m}{\lambda_t} \right)^{2/3}, \quad (20)$$

$$c_2 = 0.5[Q_{a,\text{ADDA}}(\lambda_t) - Q_{a,\text{IGOM}}(\lambda_t)] \left( \frac{\pi D_m}{\lambda_t} \right)^{2/3}, \quad (21)$$

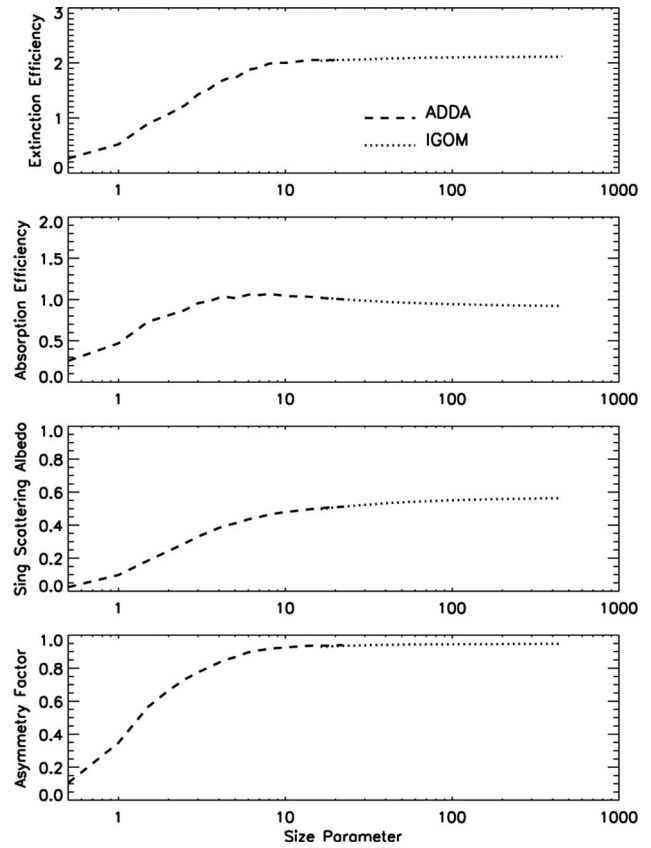


Fig. 6. Same as Fig. 5, except that  $\lambda = 12.0 \mu\text{m}$ . The refractive index of ice at  $\lambda = 12.0 \mu\text{m}$  is  $1.2799 + i4.13 \times 10^{-1}$ .

where  $Q_{e,\text{ADDA}}(\lambda_t)$  and  $Q_{a,\text{ADDA}}(\lambda_t)$  are the extinction and absorption efficiencies computed by the ADDA, and  $Q_{e,\text{IGOM}}(\lambda_t)$  and  $Q_{a,\text{IGOM}}(\lambda_t)$  are the efficiencies computed from the IGOM without accounting for the above-edge effect. The results in Fig. 5 indicate that the extinction efficiency for the aggregate initially rises rapidly with particle size, and it subsequently approaches a constant value of 2 with a decaying oscillation. As the size parameter increases from 40 to 1000, the absorption efficiency increases dramatically due to the increase of the ray path length within the particle, and the single-scattering albedo decreases from 1. The asymmetry factor in Fig. 5 generally increases with particle size when diffraction becomes significant compared to the scattering of light by the particle. For wavelengths with strong absorption within the particle, the scattering properties increase with particle size, as shown in Fig. 6. The results in Figs. 5 and 6 reflect smooth transitions of the scattering properties from small to large particles, although a small difference in the asymmetry factors is apparent when  $\lambda = 2.13 \mu\text{m}$ . Because of improvements in the IGOM, the computations by the ADDA and IGOM are very consistent in the region where the size parameter is approximately 25. The scattering properties of the aggregates in our study are computed by the ADDA when the size parameter is smaller than 25, and they



are computed by the IGOM for aggregates with larger size parameters.

Figure 7 shows the scattering phase matrices for aggregate 1 with a maximum dimension of  $100\text{ }\mu\text{m}$ . In the manner of Yang and Liou [8], the surface roughness of the aggregates is specified by many small tilted facets on the particle surface. The slopes of the roughened facets are randomly sampled assuming a Gaussian distribution [54]. The rms tilt  $\sigma$  can be used as the parameter to specify the degree of surface roughness. As  $\sigma$  increases from 0 to 1, the surface roughness varies from smooth to deeply roughened. As shown in Fig. 7, aggregates are seen to be associated with strong forward scattering at VIS wavelengths due to diffraction. In addition, the phase function for a smooth aggregate reveals halo peaks at approximately  $22^\circ$  and  $46^\circ$ . However, the maxima of the halos decrease as  $\sigma$  increases because of spreading of the rays associated with the minimum deviation of refraction. Figure 8 shows the independent nonzero elements of the scattering phase matrix for aggregate 10 with a maximum dimension of  $1000\text{ }\mu\text{m}$ . The scattering phase function ( $P_{11}$ ) for aggregate 10 has lower values at some side scattering angles compared to aggregate 1 for smooth particles, but these differences decrease as  $\sigma$  increases. It is interesting to note that an increasing  $\sigma$  tends to increase the side scattering over that of smooth particles. Additionally, the other independent nonzero elements of the phase matrices in Figs. 7 and 8 are sensitive to ice particle habit, size, and surface roughness, which indicate the potential of using polarization measurements to determine ice cloud microphysical properties. Figure 9 compares the scattering phase matrices for aggregates 1 and

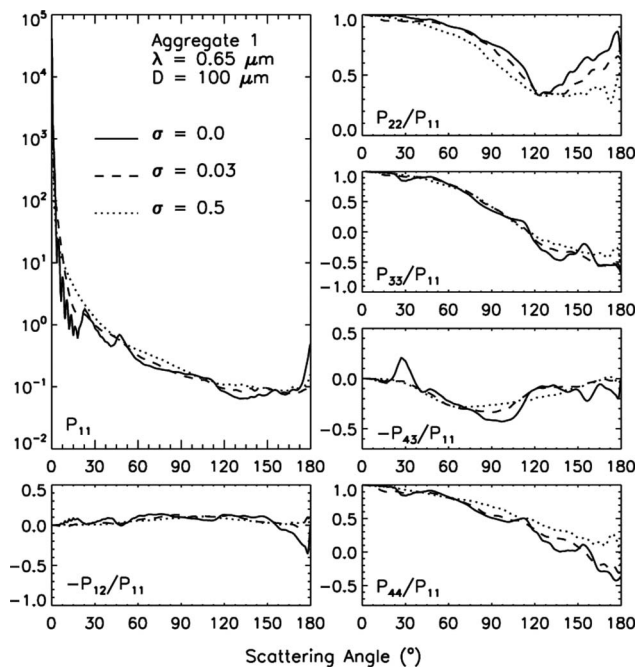


Fig. 7. Scattering phase matrices for aggregate 1 at  $\lambda = 0.65\text{ }\mu\text{m}$ . The refractive index of ice at  $\lambda = 0.65\text{ }\mu\text{m}$  is  $1.3080 + i1.43 \times 10^{-8}$ .

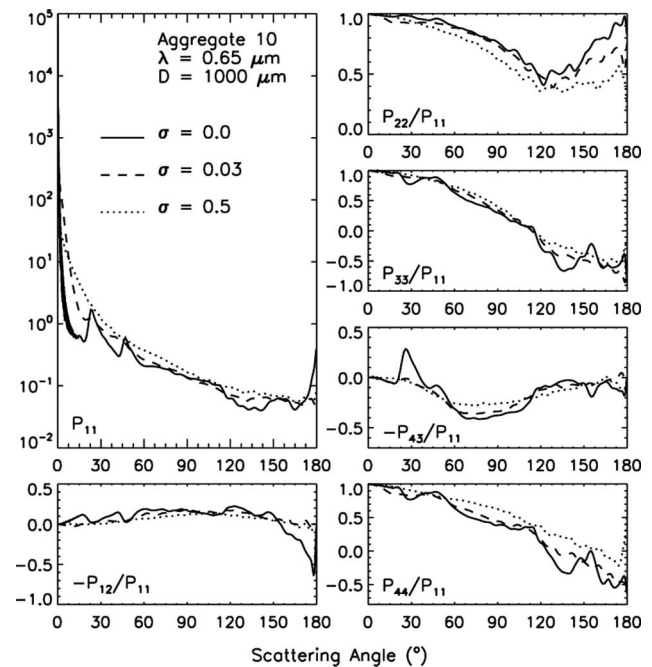


Fig. 8. Scattering phase matrices for aggregate 10 at  $\lambda = 0.65\text{ }\mu\text{m}$ . The refractive index of ice at  $\lambda = 0.65\text{ }\mu\text{m}$  is  $1.3080 + i1.43 \times 10^{-8}$ .

10 at  $\lambda = 12.0\text{ }\mu\text{m}$ , and it can be seen that the various elements of the phase matrix tend to be nearly featureless (i.e., no halos) because of strong absorption.

#### 4. Sensitivity of the Aggregate Ensemble Representation

Various aggregate models consisting of either one or a small number of predetermined geometric particles have been used in previous studies [8,20,22,28]. Our

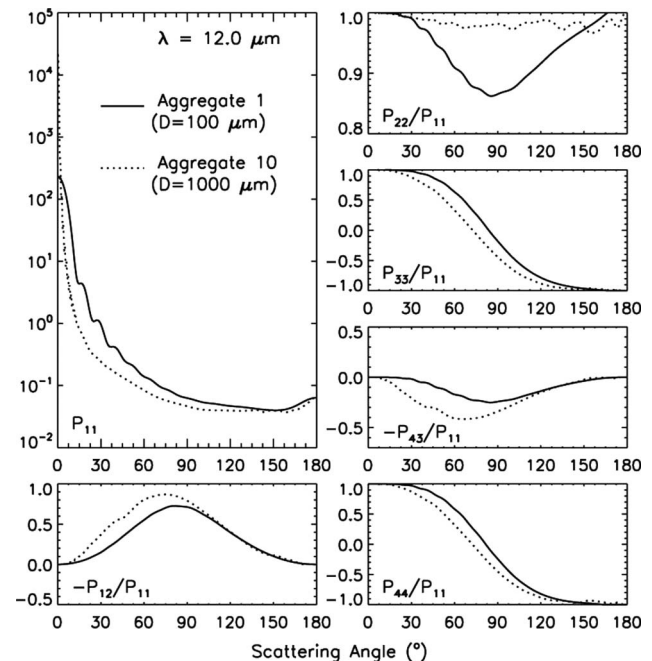


Fig. 9. Scattering phase matrices for aggregates 1 and 10 at  $\lambda = 12.0\text{ }\mu\text{m}$ . The refractive index of ice at  $\lambda = 12.0\text{ }\mu\text{m}$  is  $1.2799 + i4.13 \times 10^{-1}$ .

aggregate representation uses 10 aggregate geometries with various particle sizes to represent the aggregates found in ice clouds. The averaged scattering properties of the ice cloud aggregates can be used to investigate the ability of our aggregate model to represent an ensemble of particles.

Figure 10 shows the comparison of the scattering phase functions for the “aggregates” contained in ice clouds with the approximations using our aggregate representations shown in Figs. 2 and 3. To represent the variety of aggregates in ice clouds, the “aggregates” are an average of 1000 computer-generated aggregates

composed of four or five hexagonal plates having aspect ratios as described by Eq. (1). Similar to the aggregate representation involving aggregates 6–10, large aggregates in the “aggregates” consist of 8 to 12 plates, except that 1000 geometries are considered. The equivalent phase functions in Fig. 10 are given by

$$\overline{P_{11}(\Theta, D_m, \lambda)} = \frac{\sum_{n=1}^M P_{11}(\Theta, D_m, \lambda, n) C_s(D_m, \lambda, n)}{\sum_{n=1}^M C_s(D_m, \lambda, n)}, \quad (22)$$

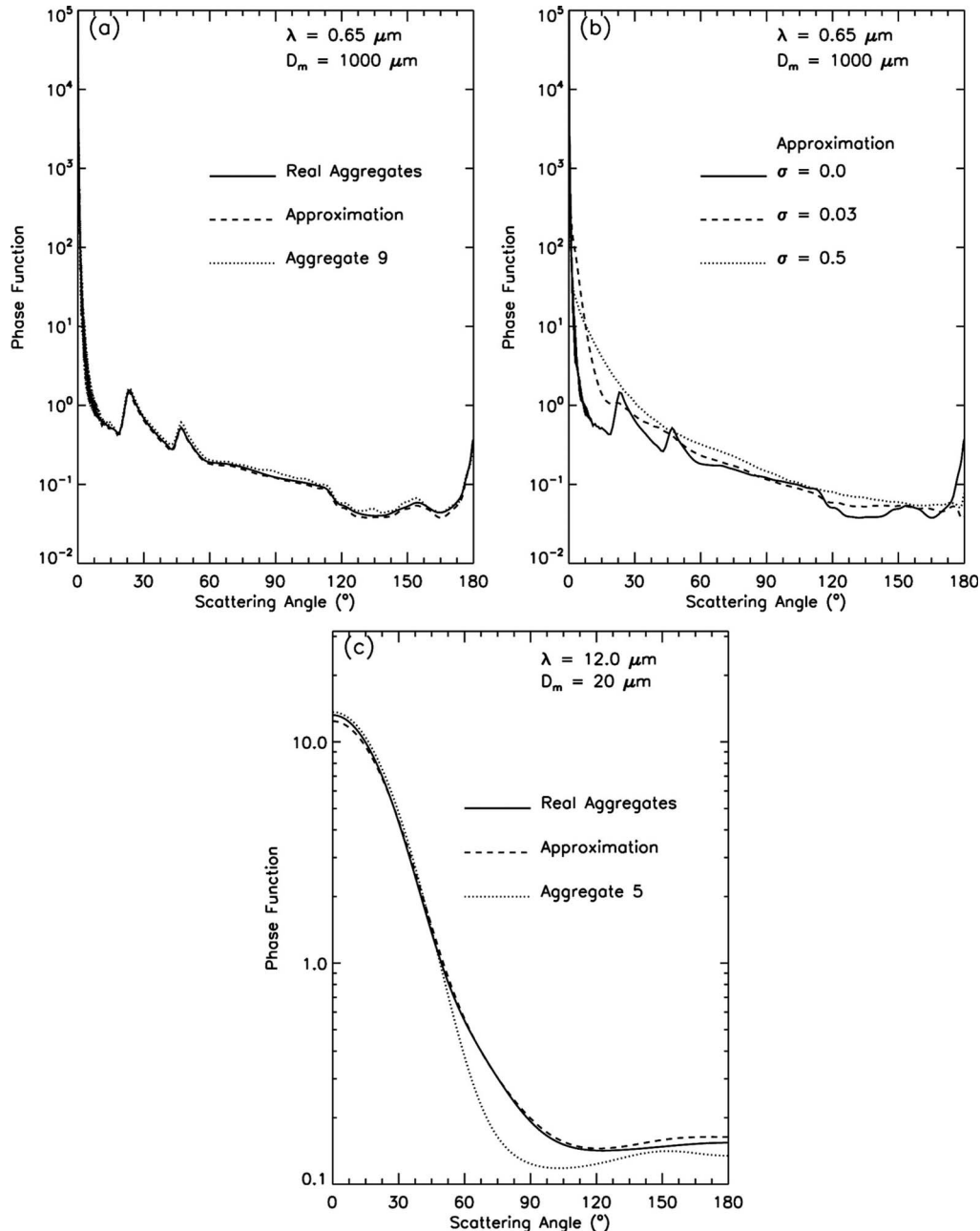


Fig. 10. (a) Comparison of the scattering phase functions for the averaged values over 1000 aggregates (solid curve), the approximation using aggregates 6–10 (dashed curve), and aggregate 9 (dotted curve). (b) Comparison of the scattering phase functions for ice crystal surface under smooth, moderately rough, and very rough conditions. (c) Comparison of the scattering phase functions for the averaged values over 1000 aggregates (solid curve), the approximation using aggregates 1–5 (dashed curve), and aggregate 5 (dotted curve).

where  $P_{11}(\Theta, D_m, \lambda, n)$  is the phase function for each aggregate geometry,  $\Theta$  is the scattering angle,  $C_s(D_m, \lambda, n)$  is the scattering cross section, and  $M$  is 5 and 1000 for our aggregate representation and the “aggregates,” respectively. Figure 10(a) illustrates the comparison of the scattering phase functions for large aggregates at  $\lambda = 0.65 \mu\text{m}$ . The results indicate that the phase function of a large aggregate shows a slight sensitivity to particle geometry. Generally, for large particles, both aggregate 9 and the “aggregates” are consistent in their representation of scattering properties. However, tiny oscillations are noticeable in the phase function of a single aggregate, especially at small scattering angles. In the “aggregates” and our aggregate representation, these oscillations are averaged to be physically more meaningful. Figure 10(b) compares the phase functions of our aggregate representation for various surface roughness conditions. The phase function oscillation is reduced greatly when surface roughness is incorporated. The aggregates being considered in Fig. 10(c) are represented by aggregate 5, aggregates 1–5, and the “aggregates.” The scattering phase functions are computed by the ADDA because the size parameter is small. In the comparison between the phase functions of the “aggregates” and aggregate 5, slight differences are shown in the forward scattering region. At side and back scattering angles, the phase function of aggregate 5 is substantially different from those of the other two aggregate representations. The Student’s  $t$ -test [55] is used to investigate the difference between the phase functions from the two aggregate representations. The  $t$ -test is used because the goal is to compare the phase functions averaged over both 10 and 1000 aggregate geometries and subsequently determine if 10 aggregates can be used to represent the 1000 aggregates. The use of fewer aggregate representations greatly decreases the amount of computer time necessary to calculate the scattering properties. The samples of the Student’s  $t$ -test are the averaged phase functions as functions of the scattering angle. Therefore, the Student’s  $t$ -test can provide an estimate of the overall agreement of the phase functions from the 1000 aggregates and the approximation using 10 aggregates.

gates” containing 1000 geometries. The Student’s  $t$ -test can be carried out on the phase functions of the “aggregates” and our aggregate representation. To assess the significance of our aggregate representation, the  $t$ -statistics are computed as follows:

$$|t| = 0.1405 < t_{0.05} = 1.96, \quad (23)$$

$$|t| = 0.5096 < t_{0.05} = 1.96, \quad (24)$$

for the phase functions at the scattering angles of  $0^\circ$ – $180^\circ$  and  $60^\circ$ – $180^\circ$ , respectively. The null hypothesis is rejected in favor of the alternative hypothesis. Therefore, the aggregate representation in this study can be used to represent the “aggregates” in the simulation of their scattering properties.

## 5. Aggregation Effect in the Retrieval of Ice Cloud Properties

To simulate the scattering properties of ice clouds containing individual hexagonal particles and their aggregates, we first assume the geometries shown in Figs. 2 and 3. The particle sizes of the aggregates are based on a particle size distribution, which, for ice clouds, is generally parameterized by the gamma distribution [56–58] given by

$$n(D_m) = N_0 D_m^\mu \exp\left(-\frac{b + \mu + 0.67}{D_{m\text{median}}} D_m\right), \quad (25)$$

where  $D_m$  is the dimension of the aggregate,  $N_0$  is the concentration intercept parameter, and  $D_{m\text{median}}$  is the median of the distribution of  $D_m$ . The parameters,  $\mu$  and  $b$ , are assumed to be 2.0 and 2.2, respectively [2]. Clouds containing a mixture of ice habits can be generated by the decomposition of a number of aggregates into hexagonal fractions. The geometries of the fractions are dependent on the aggregate dimensions and can be derived based on the information provided in Tables 1 and 2. The effective diameter of the ice clouds are derived as follows:

$$D_e = \frac{3}{2} \frac{(1-f) \left[ \sum_{i=1}^{24} \int_{D_{\min}}^{D_1} V_{pi} n(D_m) dD_m + \sum_{j=1}^{50} \int_{D_1}^{D_{\max}} V_{pj} n(D_m) dD_m \right] + N_a f \int_{D_{\min}}^{D_{\max}} V_a n(D_m) dD_m}{(1-f) \left[ \sum_{i=1}^{24} \int_{D_{\min}}^{D_1} A_{pi} n(D_m) dD_m + \sum_{j=1}^{50} \int_{D_1}^{D_{\max}} A_{pj} n(D_m) dD_m \right] + N_a f \int_{D_{\min}}^{D_{\max}} A_a n(D_m) dD_m}, \quad (26)$$

Aggregate 5 can be used to represent the “aggregates” when the null hypothesis is rejected. For scattering angles of  $60^\circ$ – $180^\circ$ , the  $t$ -statistic,  $|t| = 5.1862$ , has exceeded the 95% confidence level ( $t_{0.05} = 1.96$ ), which suggests that the differences in phase functions are significant between aggregate 5 and the “aggre-

gates” where  $f$  is the proportion of the plates that form aggregates;  $V_{pi}$  and  $V_{pj}$  are the volumes of the plates in Tables 1 and 2, respectively;  $A_{pi}$  and  $A_{pj}$  are the projected areas of the plates;  $V_a$  is the averaged volume of the aggregates used to represent all aggregate ice crystals;  $N_a$  is the number of the aggregate

geometries; and  $D_1$  is the threshold value of the aggregate dimensions to determine small and large aggregates. In this study,  $N_a$  is 5 and  $D_1$  is assumed to be  $550\text{ }\mu\text{m}$ . Note that the particle size distributions of plates are different than that of the aggregates. However, the size distributions of the plates are not derived because they are not used in the computation of the effective particle sizes and scattering properties in our cloud model.

can both affect the retrieval of cloud optical thickness. A reduction in the particle number concentration caused by the aggregation process tends to decrease the ice cloud optical thickness. This feature becomes more pronounced when 90% of the plates form aggregates, as shown in Fig. 11(b). It is also clear from Fig. 11 that the retrieved ice cloud effective particle sizes generally decrease when the aggregation effect is ignored in the retrieval process.

The phase functions of ice clouds are given by

$$P_{11} = \frac{(1-f) \left[ \sum_{i=1}^{24} \int_{D_{\min}}^{D_1} P_{11,pi} C_{s,pi} n(D_m) dD_m + \sum_{i=25}^{74} \int_{D_1}^{D_{\max}} P_{11,pi} C_{s,pi} n(D_m) dD_m \right] + N_a f \int_{D_{\min}}^{D_{\max}} P_{11,a} C_{s,a} n(D_m) dD_m}{(1-f) \left[ \sum_{i=1}^{24} \int_{D_{\min}}^{D_1} C_{s,pi} n(D_m) dD_m + \sum_{i=25}^{74} \int_{D_1}^{D_{\max}} C_{s,pi} n(D_m) dD_m \right] + N_a f \int_{D_{\min}}^{D_{\max}} C_{s,a} n(D_m) dD_m}, \quad (27)$$

where  $P_{11,pi}$  and  $C_{s,pi}$  are the phase function and scattering cross section for the plates and  $P_{11,a}$  and  $C_{s,a}$  are the phase function and scattering cross section for the aggregates.

To investigate the influence of ice particle aggregation on the inference of ice cloud microphysical and optical properties, reflectances are simulated by the discrete ordinates radiative transfer model [59] for two channels centered at wavelengths of  $0.65$  and  $2.13\text{ }\mu\text{m}$ . A dark (nonreflective) surface condition is assumed to eliminate the influence of surface bidirectional reflectance features. Figure 11 compares the calculated lookup tables. The dashed curves in Fig. 11(a) denote hexagonal plates, while the solid curves are used to indicate an ice cloud model that contains the same habits with the exception that 30% of the plates form aggregates. From Fig. 11(a), it can be found that the optical thicknesses of the ice clouds are reduced when aggregates are included. Based on the scattering properties of the aggregates, the optical thickness is determined by

$$\tau = (1-f) \Delta z \left[ \sum_{i=1}^{24} \int_{D_{\min}}^{D_1} C_{e,pi} n(D_m) dD_m + \sum_{i=25}^{74} \int_{D_1}^{D_{\max}} C_{e,pi} n(D_m) dD_m \right] + N_a f \Delta z \int_{D_{\min}}^{D_{\max}} C_{e,a} n(D_m) dD_m, \quad (28)$$

where  $\Delta z$  is the physical thickness of the cloud and  $C_{e,pi}$  and  $C_{e,a}$  are the extinction cross sections for the plates and aggregates. When  $f$  is 0, the optical thickness is increased to that of 100% plates. From Eq. (28), it is known that the scattering properties and particle number concentration of ice crystals

## 6. Summary

With a set of *in situ* measurements of aggregates as guidance, an algorithm is developed to efficiently define the geometries of aggregates and compute their projected areas. Aggregates result from attaching ice particle hexagonal plates together in a chainlike manner. We investigate the scattering properties of randomly oriented aggregates of plates using the ADDA and IGOM for particles whose size parameters are smaller and larger than 25, respectively. The results indicate that the scattering properties are consistent in the region where the size parameter is approximately 25. At VIS wavelengths, the scattering phase functions of the aggregates show the same typical halo peaks at scattering angles of  $22^\circ$  and  $46^\circ$  as do hexagonal ice particles. The maxima of the halos are greatly reduced when the ice crystal surface roughness is taken into account.

Using the algorithm to create geometries of aggregates and their scattering properties, an investigation was performed to explore the possibility of representing all aggregates based on the scattering properties of a more limited number of aggregate representations. To represent small aggregates, we generated five aggregate geometries, with each particle consisting of four or five hexagonal plates. Aggregates with large particles were built by increasing the monomer numbers instead of merely scaling the sizes of each monomer, and five models consisting of 8–12 plates were considered. The scattering properties of a representative aggregate were derived by averaging values over the individual aggregate geometries. To determine the ability of our aggregate representation to represent a larger number of aggregate shapes, “aggregates” were simulated from 1000 different plate aggregates, with properties compared to the use of 10 different plate



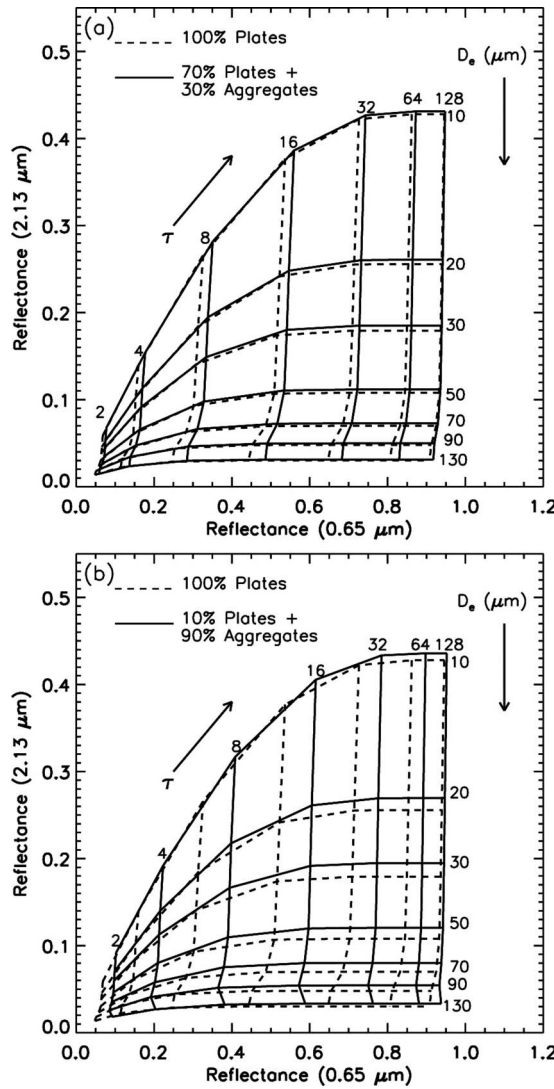


Fig. 11. Lookup tables using 0.65 (x axis) and 2.13  $\mu\text{m}$  (y axis) reflectances for (a) independent plates and the same ice crystals except that 30% plates form aggregates and (b) independent plates and the same ice crystals except that 90% plates form aggregates. The solar zenith and viewing zenith angles are 30°, respectively, and the relative azimuth angle is 90°.  $\tau$  represents the cloud optical thickness.

aggregates. The comparison of the scattering properties suggested that the variance of the phase function for an ensemble of 10 aggregate particles was small, indicating that this number of particles is sufficient to represent a larger set of particles.

Furthermore, the influence of the aggregate of plates was investigated for the satellite-based remote sensing of ice clouds. As cloud reflectances can be used to infer ice cloud microphysical and optical properties, we compared the lookup tables of cloud

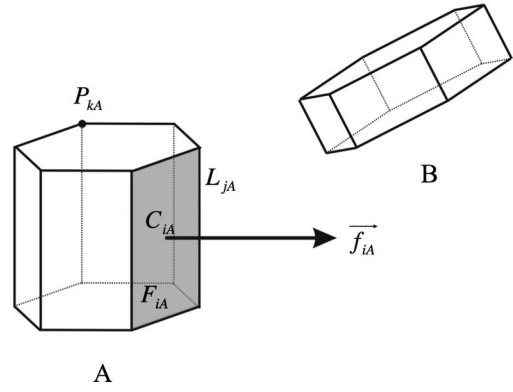


Fig. 12. Geometries of hexagonal particles.

reflectances for ice cloud models involving hexagonal plates and their aggregates. The neglect of aggregates in the retrieval process leads to an overestimate of optical thickness but an underestimate of effective particle size. This result is partly due to the lower projected areas of the ice crystals during the aggregation process. More detailed investigations of the plate aggregates need to be performed in conjunction with other ice habits.

#### Appendix A: Estimating the Relative Position of Hexagonal Particles

Figure 12 shows the geometries of hexagonal particles used in our study. In particle A, the faces, edges, and vertices of the particle are indicated by  $F_{iA}$  ( $iA = 1, 2, \dots, 8$ ),  $L_{jA}$  ( $jA = 1, 2, \dots, 18$ ), and  $P_{kA}$  ( $kA = 1, 2, \dots, 12$ ), respectively.  $\vec{c}_{iA}$  ( $iA = 1, 2, \dots, 8$ ) are the position vectors of the centers of the particle faces,  $\vec{f}_{iA}$  ( $iA = 1, 2, \dots, 8$ ) indicate the normal directions of the particle faces, and  $\vec{p}_{kA}$  ( $kA = 1, 2, \dots, 12$ ) and  $\vec{l}_{jA}$  ( $jA = 1, 2, \dots, 18$ ) are the vectors of the vertices and edges, respectively.

The distance between two hexagonal particles that are not overlapped in the  $oxyz$  coordinate can be written by

$$D = \left\langle \begin{array}{l} D(P_{kA}, F_{iB}, kA = 1, 2, \dots, 12, iB = 1, 2, \dots, 8) \\ D(P_{kB}, F_{iA}, kB = 1, 2, \dots, 12, iA = 1, 2, \dots, 8) \\ D(L_{jA}, L_{jB}, iA = 1, 2, \dots, 18, jB = 1, 2, \dots, 18) \end{array} \right\rangle, \quad (\text{A1})$$

where  $\langle \rangle$  indicates the minimum value of the variables.

$D(P_{kA}, F_{iB}, kA = 1, 2, \dots, 12, iB = 1, 2, \dots, 8)$  are the distances between a vertex ( $P_{kA}, kA = 1, 2, \dots, 12$ ) of particle A and a face ( $F_{iB}, iB = 1, 2, \dots, 8$ ) of particle B, and they can be determined by

$$D(P_{kA}, F_{iB}, kA = 1, 2, \dots, 12, iB = 1, 2, \dots, 8) = \begin{cases} |\vec{p}_{kA} - \vec{p}_u| (kA = 1, 2, \dots, 12, iB = 1, 2, \dots, 8) & \text{for } P_u \in F_{iB} \\ \langle D(P_{kA}, L_{iBm1}, m1 = 1, 2, \dots, 4(\text{or } 6)) \rangle (kA = 1, 2, \dots, 12, iB = 1, 2, \dots, 8) & \text{for } P_u \notin F_{iB} \end{cases}, \quad (\text{A2})$$



where  $L_{iBm1}$  represents the edges on face  $F_{iB}$  and  $\vec{p}_u$  is the position vector of  $P_u$  and can be given by

$$\vec{p}_u = \vec{p}_{kA} + \vec{f}_{iB} \frac{\vec{f}_{iB} \cdot (\vec{c}_{iB} - \vec{p}_{kA})}{|\vec{f}_{iB}|^2}. \quad (\text{A3})$$

The distance between  $P_{kA}$  and  $L_{iBm1}$  can be derived as follows:

$$D(P_{kA}, L_{iBm1}, m1 = 1, 2, \dots, 4(\text{or } 6)) = \begin{cases} |\vec{p}_{kA} - \vec{p}_v| & \text{for } P_v \in L_{iBm1}, \\ \langle |\vec{p}_{kA} - \vec{p}_{iBm1m2}| (m2 = 1 \text{ and } 2) \rangle (m1 = 1, 2, \dots, 4(\text{or } 6)) & \text{for } P_v \notin L_{iBm1}, \end{cases} \quad (\text{A4})$$

where  $P_{iBm1m2}$  represents the vertices on  $L_{iBm1}$  and  $\vec{p}_v$  is the position vector of  $P_v$  and can be given by

$$\vec{p}_v = \frac{(\vec{p}_{kA} - \vec{p}_{iBm1m2}) \cdot (\vec{p}_{iBm11} - \vec{p}_{iBm12})}{|\vec{p}_{iBm11} - \vec{p}_{iBm12}|^2} (\vec{p}_{iBm11} - \vec{p}_{iBm12}) + \vec{p}_{iBm11} \quad (m1 = 1, 2, \dots, 4(\text{or } 6)). \quad (\text{A5})$$

$D(L_{jA}, L_{jB}, jA = 1, 2, \dots, 18, jB = 1, 2, \dots, 18)$  in Eq. (A1) is the distance between  $L_{jA}$  ( $jA = 1, 2, \dots, 18$ ) and  $L_{jB}$  ( $jB = 1, 2, \dots, 18$ ) from particles A and B, respectively, and can be given as follows:

$$D(L_{jA}, L_{jB}, jA = 1, 2, \dots, 18, jB = 1, 2, \dots, 18) = \begin{cases} |\vec{p}_{jAm3} - \vec{p}_{jBm4}| (m3, m4 = 1 \text{ and } 2) \\ D(P_{jAm3}, L_{jB}, m3 = 1 \text{ and } 2) \\ D(P_{jBm4}, L_{jA}, m4 = 1 \text{ and } 2) \\ D(P_w, L_{jA}) \text{ for } P_w \in L_{jB} \end{cases}, \quad (\text{A6})$$

where  $D(P_{jAm3}, L_{jB}, m3 = 1 \text{ and } 2)$  and  $D(P_{jBm4}, L_{jA}, m4 = 1 \text{ and } 2)$  can be derived from Eq. (A4). The position vector of the  $P_w$  in Eq. (A6) is given by

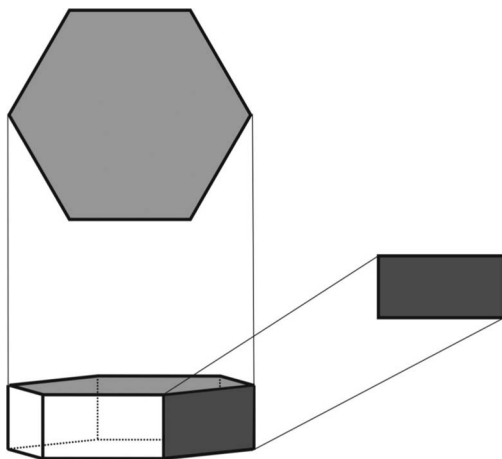


Fig. 13. Two types of faces for a hexagonal ice crystal.

$$\vec{P}_w = \vec{p}'_{jA1} + (\vec{p}'_{jA1} - \vec{p}'_{jA2}) \frac{[(\vec{p}'_{jA1} - \vec{p}_{jB1}) \times (\vec{p}_{jB2} - \vec{p}_{jB1})] \cdot [(\vec{p}'_{jA2} - \vec{p}'_{jA1}) \times (\vec{p}_{jB2} - \vec{p}_{jB1})]}{[(\vec{p}'_{jA2} - \vec{p}'_{jA1}) \times (\vec{p}_{jB2} - \vec{p}_{jB1})] \cdot [(\vec{p}'_{jA2} - \vec{p}'_{jA1}) \times (\vec{p}_{jB2} - \vec{p}_{jB1})]_z}, \quad (\text{A7})$$

where

$$\vec{p}'_{jA1} = \vec{p}_{jA1} + (\vec{l}_{jA} \times \vec{l}_{jB}) \frac{(\vec{l}_{jA} \times \vec{l}_{jB}) \cdot (\vec{p}_{jB1} - \vec{p}_{jA1})}{|\vec{l}_{jA} \times \vec{l}_{jB}|^2}, \quad (\text{A8})$$

$$\vec{p}'_{jA2} = \vec{p}_{jA2} + (\vec{l}_{jA} \times \vec{l}_{jB}) \frac{(\vec{l}_{jA} \times \vec{l}_{jB}) \cdot (\vec{p}_{jB1} - \vec{p}_{jA2})}{|\vec{l}_{jA} \times \vec{l}_{jB}|^2}. \quad (\text{A9})$$

Particles A and B are not overlapped in space if they satisfy

$$\begin{cases} \sum_{iB=1}^8 D(P_{kA}, F_{iB}, kA = 1, 2, \dots, 12) \neq 3\sqrt{3}a_B + L_B \\ \sum_{iA=1}^8 D(P_{kB}, F_{iA}, kB = 1, 2, \dots, 12) \neq 3\sqrt{3}a_A + L_A, \\ \sum_{jA=1}^{18} L_{jA} \cap \sum_{iB=1}^8 F_{iB} = \emptyset \end{cases} \quad (\text{A10})$$

where  $a_A$  and  $a_B$  and  $L_A$  and  $L_B$  are the semiwidths and lengths of the hexagonal particles, respectively.

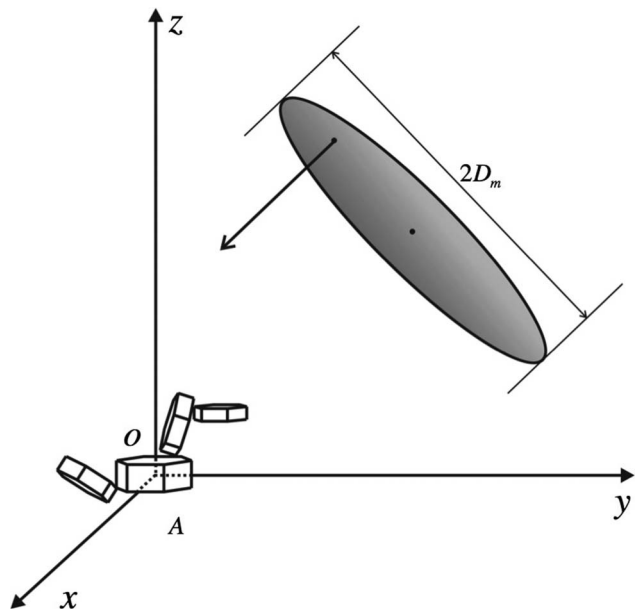


Fig. 14. Schematic illustrating the computation of the projected area of an aggregate ice crystal.

The derivation of  $D(P_{kA}, F_{iB}, kA = 1, 2, \dots, 12, iB = 1, 2, \dots, 8)$  and  $D(P_{kB}, F_{iA}, kB = 1, 2, \dots, 12, iA = 1, 2, \dots, 8)$  can be found in Eqs. (A1) and (A2). Figure 13 shows two types  $F_{iB}$ . If  $F_{iB}$  has a rectangular shape, the relationship between  $L_{jA}$  and  $F_{iB}$  in Eq. (A10) can be derived as follows:

$$\begin{cases} L_{jA} \cap F_{iB} \neq \emptyset & \text{for } \sum_{m5=1}^4 D(L_{jA}, L_{iBm5}) \neq a_B + L_B \\ L_{jA} \cap F_{iB} = \emptyset & \text{for } \sum_{m5=1}^4 D(L_{jA}, L_{iBm5}) = a_B + L_B \end{cases}, \quad (\text{A11})$$

where  $D(L_{jA}, L_{iBm5}, m5 = 1, 2, \dots, 4)$  is the distance between  $L_{jA}$  and the boundaries of  $F_{iB}$ . The derivation of  $D(L_{jA}, L_{iBm5}, m5 = 1, 2, \dots, 4)$  can be found in Eq. (A6). If  $F_{iB}$  has the hexagonal structure shown in Fig. 13,  $L_{jA} \cap F_{iB}$  can be given by

$$\begin{cases} L_{jA} \cap F_{iB} \neq \emptyset & \text{for } \sum_{m6=1}^6 D(L_{jA}, L_{iBm6}) \neq 3\sqrt{3}a_B \\ L_{jA} \cap F_{iB} = \emptyset & \text{for } \sum_{m6=1}^6 D(L_{jA}, L_{iBm6}) = 3\sqrt{3}a_B \end{cases}. \quad (\text{A12})$$

## Appendix B: Compute Projected Area of an Aggregate

Figure 14 shows aggregate A in the  $oxyz$  coordinate system. The projected area of an aggregate can be computed by an algorithm based on the Monte Carlo method. Consider a random disk  $D_i$  that is perpendicular to its center position vector  $\vec{p}_{i0}$ . The radius of  $D_i$  is equal to the maximum dimension of the aggregate  $D_m$ , and a random point  $P_i$  on the disk can be derived from

$$|\vec{p}_i - \vec{p}_{i0}| = D_m \sqrt{\xi_A}, \quad (\text{B1})$$

$$\vec{p}_i \cdot \vec{p}_{i0} = |\vec{p}_{i0}|^2, \quad (\text{B2})$$

$$(\vec{p}_i - \vec{p}_{i0}) \cdot (\vec{p}_B - \vec{p}_{i0}) = D_m \sqrt{\xi_A} |\vec{p}_B - \vec{p}_{i0}| \cos(2\pi\xi_B), \quad (\text{B3})$$

where  $\xi_A$  and  $\xi_B$  are independent random numbers that are uniformly distributed on  $[0, 1]$  and  $\vec{p}_B$  is the position vector of a fixed point on the face containing  $D_i$  and can be given by

$$\vec{p}_B = \left( 0, 0, \frac{|\vec{p}_{i0}|^2}{(\vec{p}_{i0})_z} \right). \quad (\text{B4})$$

For a line  $L_i$  that satisfies

$$\begin{cases} P_i \in L_i \\ \vec{l}_i = \vec{p}_{i0} \end{cases}, \quad (\text{B5})$$

we consider a  $M_i$  given by

$$M_i = \begin{cases} 1 & \text{for } L_i \cap \sum_{j=1}^{8N} F_j \neq \emptyset \\ 0 & \text{for } L_i \cap \sum_{j=1}^{8N} F_j = \emptyset \end{cases}, \quad (\text{B6})$$

where  $F_j$  indicates a face of aggregate A in Fig. 14 and  $N$  is the number of the hexagonal particles in

A. The relationship between  $L_i$  and  $F_j$  can be derived using Eqs. (A11) and (A12).

The projected area of aggregate A can be derived by

$$S = \pi D_m^2 \frac{\sum_{i=1}^N M_i}{N_L}, \quad (\text{B7})$$

where  $N_L$  is the number of  $D_i$  in the computation. The algorithm to compute the projected area can be verified by replacing aggregate A with a hexagonal column whose projected area can be simply determined by

$$S = \frac{3}{4}a \left( \sqrt{3}a + 2L \right), \quad (\text{B8})$$

where  $a$  and  $L$  represent the semiwidth and length of the hexagonal column, respectively. This result is obtained by using the fact that the projected area of a convex body at random orientation is simply one-fourth of its surface area. Our results indicate that the projected area of an aggregate can be accurately computed for the case  $N_L > 100,000$ .

This research is supported by a research grant from National Aeronautics and Space Administration (NASA) (NNX08AF68G) from the NASA Radiation Sciences Program managed by Hal Maring and the MODIS Program managed by Paula Bontempi. This study was also partly supported by a subcontract G074605 issued by the University of Wisconsin to Texas A&M University. George W. Kattawar's research is also supported by the Office of Naval Research (ONR) under contract N00014-06-1-0069. Bryan Baum gratefully acknowledges the support provided through NASA grant NNX08AF81G.

## References

1. B. A. Baum, A. J. Heymsfield, P. Yang, and S. T. Bedka, "Bulk scattering properties for the remote sensing of ice clouds. part I: microphysical data and models," *J. Appl. Meteorol.* **44**, 1885–1895 (2005).
2. B. A. Baum, P. Yang, A. J. Heymsfield, S. Platnick, M. D. King, Y. X. Hu, and S. T. Bedka, "Bulk scattering properties for the remote sensing of ice clouds. part II: narrowband models," *J. Appl. Meteorol.* **44**, 1896–1911 (2005).
3. A. J. Baran, "A review of the light scattering properties of cirrus," *J. Quant. Spectrosc. Radiat. Transfer* **110**, 1239–1260 (2009).
4. C. G. Schmitt and A. J. Heymsfield, "The dimensional characteristics of ice crystal aggregates from fractal geometry," *J. Atmos. Sci.* **67**, 1605–1616 (2010).
5. P. Yang, Z. B. Zhang, G. W. Kattawar, S. G. Warren, B. A. Baum, H. L. Huang, Y. X. Hu, D. Winker, and J. Iaquinta, "Effect of cavities on the optical properties of bullet rosettes: implications for active and passive remote sensing of ice cloud properties," *J. Appl. Meteorol. Clim.* **47**, 2311–2330 (2008).
6. W. Tape, *Atmospheric Halos*, Antarctic Research Series (American Geophysical Union, 1994), p. 143.

7. A. Macke, J. Mueller, and E. Raschke, "Single scattering properties of atmospheric ice crystals," *J. Atmos. Sci.* **53**, 2813–2825 (1996).
8. P. Yang and K. N. Liou, "Single-scattering properties of complex ice crystals in terrestrial atmosphere," *Contrib. Atmos. Phys.* **71**, 223–248 (1998).
9. V. Shcherbakov, J. F. Gayet, B. Baker, and P. Lawson, "Light scattering by single natural ice crystals," *J. Atmos. Sci.* **63**, 1513–1525 (2006).
10. P. Yang, G. Hong, G. W. Kattawar, P. Minnis, and Y. X. Hu, "Uncertainties associated with the surface texture of ice particles in satellite-based retrieval of cirrus clouds. part II: effect of particle surface roughness on retrieved cloud optical thickness and effective particle size," *IEEE Trans. Geosci. Remote Sensing* **46**, 1948–1957 (2008).
11. P. Yang, G. W. Kattawar, G. Hong, P. Minnis, and Y. X. Hu, "Uncertainties associated with the surface texture of ice particles in satellite-based retrieval of cirrus clouds. part I: single-scattering properties of ice crystals with surface roughness," *IEEE Trans. Geosci. Remote Sensing* **46**, 1940–1947 (2008).
12. M. Kajikawa and A. J. Heymsfield, "Aggregation of ice crystals in cirrus," *J. Atmos. Sci.* **46**, 3108–3121 (1989).
13. J. L. Stith, J. E. Dye, A. Bansemer, A. J. Heymsfield, C. A. Grainger, W. A. Petersen, and R. Cifelli, "Microphysical observations of tropical clouds," *J. Appl. Meteorol.* **41**, 97–117 (2002).
14. J. L. Stith, J. A. Haggerty, A. Heymsfield, and C. A. Grainger, "Microphysical characteristics of tropical updrafts in clean conditions," *J. Appl. Meteorol.* **43**, 779–794 (2004).
15. A. J. Heymsfield, "Ice particle evolution in the anvil of a severe thunderstorm during CCOPE," *J. Atmos. Sci.* **43**, 2463–2478 (1986).
16. M. W. Gallagher, P. J. Connolly, J. Whiteway, D. Figueras-Nieto, M. Flynn, T. W. Choularton, K. N. Bower, C. Cook, R. Busen, and J. Hacker, "An overview of the microphysical structure of cirrus clouds observed during EMERALD-1," *Q. J. R. Meteorol. Soc.* **131**, 1143–1169 (2005).
17. P. J. Connolly, C. P. R. Saunders, M. W. Gallagher, K. N. Bower, M. J. Flynn, T. W. Choularton, J. Whiteway, and R. P. Lawson, "Aircraft observations of the influence of electric fields on the aggregation of ice crystals," *Q. J. R. Meteorol. Soc.* **131**, 1695–1712 (2005).
18. G. M. McFarquhar and A. J. Heymsfield, "Microphysical characteristics of three anvils sampled during the Central Equatorial Experiment," *J. Atmos. Sci.* **53**, 2401–2423 (1996).
19. R. A. Houze and D. D. Churchill, "Mesoscale organization and cloud microphysics in a Bay of Bengal depression," *J. Atmos. Sci.* **44**, 1845–1867 (1987).
20. K. F. Evans, J. R. Wang, P. E. Racette, G. Heymsfield, and L. H. Li, "Ice cloud retrievals and analysis with the compact scanning submillimeter imaging radiometer and the cloud radar system during CRYSTAL FACE," *J. Appl. Meteorol.* **44**, 839–859 (2005).
21. J. Um and G. M. McFarquhar, "Single-scattering properties of aggregates of bullet rosettes in cirrus," *J. Appl. Meteorol. Clim.* **46**, 757–775 (2007).
22. J. Um and G. M. McFarquhar, "Single-scattering properties of aggregates of plates," *Q. J. R. Meteorol. Soc.* **135**, 291–304 (2009).
23. A. J. Baran, V. N. Shcherbakov, B. A. Baker, J. F. Gayet, and R. P. Lawson, "On the scattering phase-function of non-symmetric ice-crystals," *Q. J. R. Meteorol. Soc.* **131**, 2609–2616 (2005).
24. P. Dinh-Van and L. Phan-Cong, "Aggregation of small ice crystals in an electric field," *Atmos.-Ocean* **16**, 248–259 (1978).
25. H. R. Pruppacher, "The effects of electric fields on cloud physical processes," *J. Appl. Math. Phys.* **14**, 590–599 (1963).
26. P. Hobbs, S. Chang, and J. Locatelli, "The dimension and aggregation of ice crystals in natural clouds," *J. Geophys. Res.* **79**, 2199–2206 (1974).
27. R. P. Lawson, B. A. Baker, C. G. Schmitt, and T. L. Jensen, "An overview of microphysical properties of Arctic clouds observed in May and July 1998 during FIRE ACE," *J. Geophys. Res.* **106**, 14989–15014 (2001).
28. A. J. Baran and L. C. Labonnote, "On the reflection and polarisation properties of ice cloud," *J. Quant. Spectrosc. Radiat. Transfer* **100**, 41–54 (2006).
29. B. T. Draine, "The discrete dipole approximation and its application to interstellar graphite grains," *Astrophys. J.* **333**, 848–872 (1988).
30. E. M. Purcell and C. R. Pennypacker, "Scattering and absorption of light by nonspherical dielectric grains," *Astrophys. J.* **186**, 705–714 (1973).
31. F. M. Kahnert, "Numerical methods in electromagnetic scattering theory," *J. Quant. Spectrosc. Radiat. Transfer* **79**, 775–824 (2003).
32. K. F. Evans and G. L. Stephens, "Microwave radiative transfer through clouds composed of realistically shaped ice crystals. part I: single scattering properties," *J. Atmos. Sci.* **52**, 2041–2057 (1995).
33. Q. Cai and K. N. Liou, "Polarized-light scattering by hexagonal ice crystals: theory," *Appl. Opt.* **21**, 3569–3580 (1982).
34. A. Macke, "Scattering of light by polyhedral ice crystals," *Appl. Opt.* **32**, 2780–2788 (1993).
35. H. R. Pruppacher and J. D. Klett, *Microphysics of Clouds and Precipitation* (Reidel, 1980).
36. M. A. Yurkin, V. P. Maltsev, and A. G. Hoekstra, "The discrete dipole approximation for simulation of light scattering by particles much larger than the wavelength," *J. Quant. Spectrosc. Radiat. Transfer* **106**, 546–557 (2007).
37. M. A. Yurkin and A. G. Hoekstra, "User manual for the discrete dipole approximation code ADDA v. 0.79," [http://a-dda.googlecode.com/svn/tags/rel\\_0\\_79/doc/manual.pdf](http://a-dda.googlecode.com/svn/tags/rel_0_79/doc/manual.pdf) (2009).
38. B. T. Draine and P. J. Flatau, "Discrete-dipole approximation for scattering calculations," *J. Opt. Soc. Am. A* **11**, 1491–1499 (1994).
39. B. T. Draine and J. Goodman, "Beyond Clausius–Mossotti—wave propagation on a polarizable point lattice and the discrete dipole approximation," *Astrophys. J.* **405**, 685–697 (1993).
40. P. Yang and K. N. Liou, "Geometric-optics-integral-equation method for light scattering by nonspherical ice crystals," *Appl. Opt.* **35**, 6568–6584 (1996).
41. O. V. Kalashnikova and I. N. Sokolik, "Modeling the radiative properties of nonspherical solid-derived mineral aerosols," *J. Quant. Spectrosc. Radiat. Transfer* **87**, 137–166 (2004).
42. L. Bi, P. Yang, G. W. Kattawar, and R. Kahn, "Single-scattering properties of triaxial ellipsoidal particles for a size parameter range from the Rayleigh to geometric-optics regimes," *Appl. Opt.* **48**, 114–126 (2009).
43. G. Hong, P. Yang, B. A. Baum, A. J. Heymsfield, F. Z. Weng, Q. H. Liu, G. Heygster, and S. A. Buehler, "Scattering database in the millimeter and submillimeter wave range of 100–1000 GHz for nonspherical ice particles," *J. Geophys. Res.* **114**, D06201, doi:06210.01029/02008JD010451 (2009).
44. T. Nousiainen, E. Zubko, J. V. Niemi, K. Kupiainen, M. Lehtinen, K. Muinonen, and G. Videen, "Single-scattering modeling of thin, birefringent mineral-dust flakes using the discrete-dipole approximation," *J. Geophys. Res.* **114**, D07207, doi:07210.01029/02008JD011564 (2009).
45. T. Nousiainen and K. Muinonen, "Surface-roughness effect on single-scattering properties of wavelength-scale particles," *J. Quant. Spectrosc. Radiat. Transfer* **106**, 389–397 (2007).

46. K.-N. Liou, *An Introduction to Atmospheric Radiation*, 2nd ed., International geophysics series Vol. 84 (Academic, 2002), pp. xiv, 583.
47. M. Wendisch, P. Pilewskie, J. Pommier, S. Howard, P. Yang, A. J. Heymsfield, C. G. Schmitt, D. Baumgardner, and B. Mayer, "Impact of cirrus crystal shape on solar spectral irradiance: a case study for subtropical cirrus," *J. Geophys. Res.* **110**, D03202, doi:03210.01029/02004JD005294 (2005).
48. P. Yang, H. L. Wei, H. L. Huang, B. A. Baum, Y. X. Hu, G. W. Kattawar, M. I. Mishchenko, and Q. Fu, "Scattering and absorption property database for nonspherical ice particles in the near- through far-infrared spectral region," *Appl. Opt.* **44**, 5512–5523 (2005).
49. Z. B. Zhang, P. Yang, G. W. Kattawar, S. C. Tsay, B. A. Baum, Y. X. Hu, A. J. Heymsfield, and J. Reichardt, "Geometrical-optics solution to light scattering by droxtal ice crystals," *Appl. Opt.* **43**, 2490–2499 (2004).
50. C. G. Schmitt, J. Iaquinta, and A. J. Heymsfield, "The asymmetry parameter of cirrus clouds composed of hollow bullet rosette-shaped ice crystals from ray-tracing calculations," *J. Appl. Meteorol. Clim.* **45**, 973–981 (2006).
51. H. M. Nussenzweig and W. J. Wiscombe, "Efficiency factors in Mie scattering," *Phys. Rev. Lett.* **45**, 1490–1494 (1980).
52. H. M. Nussenzweig and W. J. Wiscombe, "Complex angular momentum approximation to hard-core scattering," *Phys. Rev. A* **43**, 2093–2112 (1991).
53. D. L. Mitchell, W. P. Arnott, C. Schmitt, A. J. Baran, S. Havemann, and Q. Fu, "Photon tunneling contributions to extinction for laboratory grown hexagonal columns," *J. Quant. Spectrosc. Radiat. Transfer* **70**, 761–776 (2001).
54. C. Cox and W. Munk, "Measurement of the roughness of the sea surface from photographs of the Sun's glitter," *J. Opt. Soc. Am.* **44**, 838–850 (1954).
55. D. Freedman, R. Pisani, and R. Purves, *Statistics*, 4th ed. (W. W. North, 2007).
56. A. L. Kosarev and I. P. Mazin, "An empirical model of the physical structure of upper-layer clouds," *Atmos. Res.* **26**, 213–228 (1991).
57. D. L. Mitchell, "Evolution of snow-size spectra in cyclonic storms. part II: deviations from the exponential form," *J. Atmos. Sci.* **48**, 1885–1899 (1991).
58. A. J. Heymsfield, A. Bansemer, P. R. Field, S. L. Durden, J. L. Stith, J. E. Dye, W. Hall, and C. A. Grainger, "Observations and parameterizations of particle size distributions in deep tropical cirrus and stratiform precipitating clouds: results from in situ observations in TRMM field campaigns," *J. Atmos. Sci.* **59**, 3457–3491 (2002).
59. K. Stamnes, S. C. Tsay, W. Wiscombe, and K. Jayaweera, "Numerically stable algorithm for discrete-ordinate-method radiative transfer in multiple scattering and emitting layered media," *Appl. Opt.* **27**, 2502–2509 (1988).